An Experimental Evaluation of Exhaust Nozzle/Airframe Interference

W. C. SCHNELL* AND D. MIGDAL†
Grumman Aerospace Corporation, Bethpage, N.Y.

Test results are presented to evaluate a range of nozzle types and installations for a twin-engine supersonic fighter. At subsonic, transonic, and supersonic Mach numbers, 0.6–1.3 and 2.2, simulated forebodies were mated to five aft-fuselage shapes installed with five interchangeable variable-throat nozzle types: Iris, C-D Iris, Variable Flap Ejector, Plug, and Blow-In-Door Ejector. A dual force balance system, recording static thrust, aft-fuselage drag, and over-all afterbody thrust minus drag, was used to assess the effects of engine spacing, peripheral blockage, nozzle/fuselage combination, jet area, nozzle pressure ratio, and tunnel Mach number on interference drag. The results reveal that marked reductions in high subsonic interference drag are possible with widely spaced designs and Iris type nozzles.

Introduction

PROPULSION systems claim an increasingly larger fraction of total aircraft cross-sectional area as the flight Mach number is increased and maneuvering capability is expanded. Nozzle exit area must vary over a wider range than ever before. For advanced fighters this results in nozzle boattail areas as large as 30–50% of the aircraft cross-sectional area. In such aircraft the great importance of exhaust nozzle performance requires realistic data at an early stage in the development process.

The lack of reliable analytical tools for three dimensional, viscous, multistream flows requires that most exhaust nozzle studies be done experimentally.[1–9] Maximum simulation is desirable to obtain the mutual interactions between nozzle and airframe. However, as indicated previously,[10] complete aft section thrust minus drag, by itself, is not always useful in estimating aircraft performance. New performance parameters were therefore introduced so that nozzle/airframe interacting forces could be isolated and made compatible with thrust and drag assignments.[10]

In this paper, the approach presented in Ref. 10 was implemented with a test program at the NASA Langley 16-ft transonic and 4-ft supersonic tunnels.[11,12] All of the models were built and tested in 1968. This program is the result of a joint effort among the Naval Air Systems Command, NASA Langley[13] and Grumman[14] to evaluate fighter exhaust nozzle/fuselage combinations.

Test Approach and Parameters

Currently, there are no complete simulation techniques for many future aircraft concepts. This stems from the lack of suitable microengine simulators or the absence of sufficiently large wind tunnels for complete aircraft/engine combinations. As a result, a series of partial simulation tests are required for the inlet, the aircraft, and the exhaust system. However, all such tests must be linked with suitable reference models. In this test series the aft fuselage/nozzle was simulated and a reference was employed.

The use of nozzle unbiased reference drag D_{RF} values in conjunction with static thrust measurements F_{RF} and backend thrust minus drag measurements, $(F - D)_{BE}$, leads to the following definition[10] of interference drag D_{INT}:

$$D_{INT}/F_i = (F_{RF}{}^* - D_{RF}{}^*)/F_i - (F - D)_{BE}{}^*/F_i \quad (1)$$

where the starred quantities are measured values and F_i is the ideal thrust computed by expanding the measured mass flow isentropically to ambient pressure. The measured quantities are shown schematically in Fig. 1.

In this test program, fuselage drag was obtained without nozzle flow, using a circular arc end-cap as shown in Fig. 1a, and also with a variety of nozzles at different nozzle pressure ratios $P_T/P_A = NPR$ as shown in Fig. 1c. Interference data are reported with the end-cap used to obtain D_{RF} in Eq. (1). It may also be calculated with any of the nozzles tested, from the data in Ref. 13, by using a particular D_{BE} for the reference drag.

The reference thrust (Fig. 1b) was obtained with the nozzle installed in the fuselage but without tunnel flow. Reference thrust was not affected by the aircraft design and a static

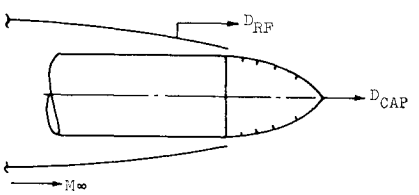

a) Reference drag—no nozzle flow

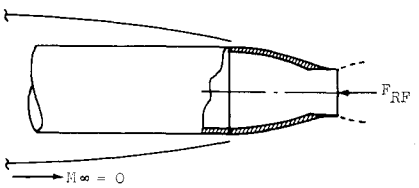

b) Reference thrust—wind tunneloff

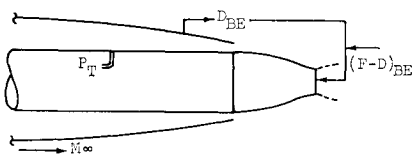

c) Aft fuselage drag and over-all afterbody thrust minus drag

Fig. 1 Measurement procedure.

Received June 4, 1969; presented as Paper 69-430 at the AIAA 5th Propulsion Joint Specialist Conference, U.S. Air Force Academy, Colo., June 9–13, 1969; revision received November 10, 1969. This work was sponsored by the Naval Air Systems Command under Contract N000 1968-C-0233.

* Propulsion Engineer. Member AIAA.
† Propulsion Project Engineer. Member AIAA.

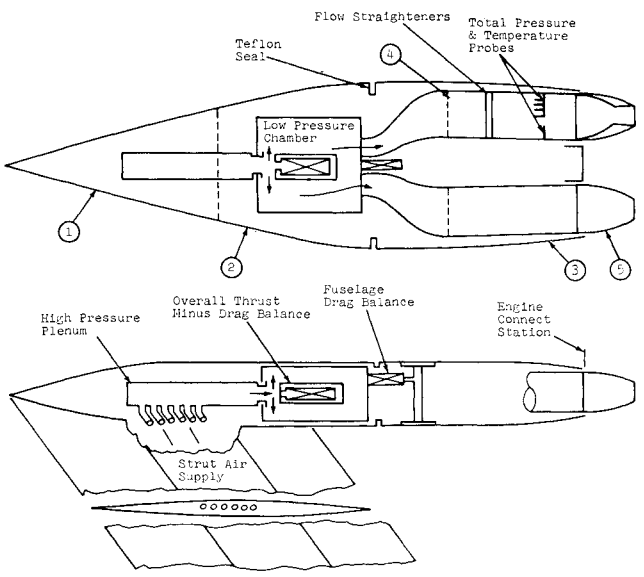

Fig. 2 Model arrangement.

thrust level was established for each nozzle independent of fuselage type.

The interference drag can also be written as

$$D_{INT}/F_i = (\Delta D + \Delta F + D_N)/F_i \quad (2)$$

with

$$\Delta D = D_{BE}^* - D_{RF}^* \quad (3)$$

$$(\Delta F + D_N)/F_i = C_V^*(F - D)_{BE}^*/F_i - D_{BE}^*/F_i \quad (4)$$

Here C_V is F_{RF}/F_i, ΔF is the loss in internal thrust (if any) due to aircraft flow, D_N is the nozzle drag, and ΔD is the difference between actual and reference back-end drag. The reason for further subdividing the interference drag [Eqs. (2–4)] is to allow a more detailed examination of the effects of nozzle on aircraft [Eq. (3)] and aircraft on nozzle [Eq. (4)].

Based on past experience (e.g., Refs. 2, 5, 9, and 12) an estimate was made of the relative magnitude of the starred quantities listed in Eqs. (1–4). Increased accuracy, for some of these drag terms, appeared possible through use of two force balances. In Eq. (1), for example, the reference drag value may be much smaller than either of the other measured quantities, yet it is a key quantity for compatibility with aircraft tests.[10] Similarly, the effect of nozzle on aircraft [ΔD in Eq. (3)] requires the difference between two low values of force. Two force balances, accurate at large and small force values, are thus ideally suited for the study of detailed effects. With a single balance system, different sections of the back-end are attached to the force balance in a series of, hopefully, identical tests. The double balance employed here measures two forces during the same test, in an arrangement developed by NASA Langley personnel.

Test Arrangement and Model Description

The over-all model arrangement shown in Fig. 2 is composed of five major sections: 1) fixed nose piece, 2) nonmetric transition section, 3) metric fuselage, 4) internal components—

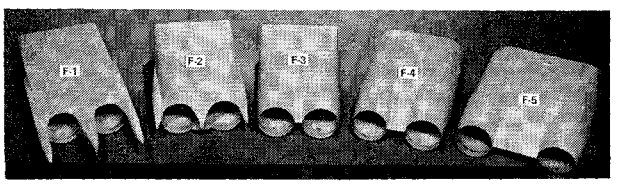

Fig. 3 Aft fuselages.

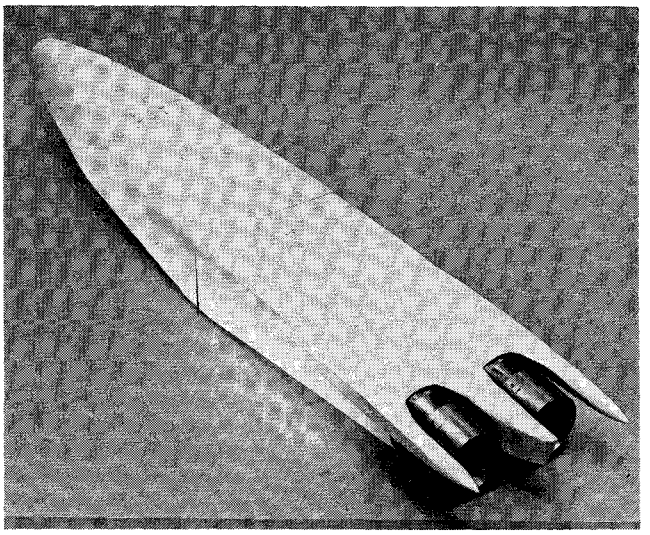

Fig. 4 A representative complete model.

air supply system and balances, and 5) metric interchangeable exhaust nozzles.

The fixed nose piece, starting with a 12° half angle, is mounted on a strut which supplies high pressure air. Three nonmetric sections, to accommodate various interengine spacings, provide the transition from the nose piece to the metric fuselages. The total nonmetric forebody (nose plus transition section) provides a simulated aircraft flowfield up to the maximum cross-sectional area station. A Teflon seal prevents cross-flow between the internal and external air at this maximum area station. The seal arrangement, devised by NASA, minimizes the transmission of axial force because of the low Teflon-on-metal friction coefficient.

Internal components are shown schematically in Fig. 2. The strut air supply enters a high pressure plenum from which it is injected normally into an annular low pressure chamber through a bellows arranged to prevent axial force transmission to the chamber. Adaptors from the chamber diffuse the flow to two internal pipes which contain orifice plates and screens to provide a uniform flow to the nozzles. The internal pipes also contain temperature and total pressure probes which, in conjunction with an upstream flow meter, were used to calculate the ideal thrust.

The dual force balance system illustrated in Fig. 2 contains a fuselage force balance which records and simultaneously transmits this force to the over-all thrust minus drag balance. Both balance recordings were corrected for extraneous loads due to a nonambient pressure in the fuselage cavity and in the step around the Teflon seal.

Figure 3 contains the five aft fuselage shapes which were tested. They include three bodies with the same interengine distance (F-1, F-2, and F-3) but with differing amounts of peripheral blockage to house aft control surfaces. The remaining fuselages (F-4 and F-5 in Fig. 3) represent designs

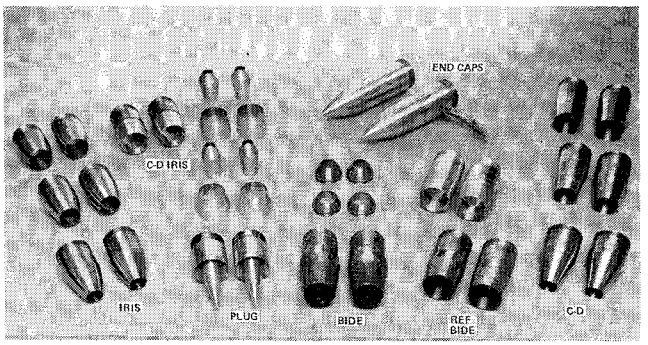

Fig. 5 Nozzles.

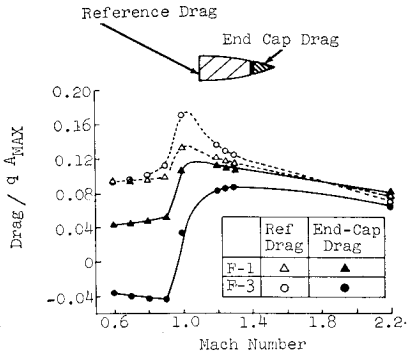

Fig. 6 Reference drag variation.

with increased interengine spacing. These fuselages represent a progressive series of fuselages with F-1 as a reference configuration. Relative to this reference, F-3 is similar in design but with less peripheral blockage, and F-3 is a clean closely-spaced design. With zero blockage, the series F-3, F-4, and F-5 is used to examine spacing effects. It should be noted that in this test series it was not feasible to remove maximum cross-sectional area with the largest spacing (F-5) because of the constraint imposed by the fixed low pressure chamber and air supply system. At the intermediate spacing (F-4) the corners at the maximum area station (Fig. 3) could be removed so that the area at this station is nearly identical with the closely-spaced designs. Figure 4 shows a typical complete model.

An array of exhaust nozzles which can be tested with all of the fuselage designs is shown in Fig. 5. These nozzles are: 1) IRIS—a variable area convergent nozzle[4] with a circular arc outer contour and a maximum boat tail angle of 22°; 2) C-D IRIS—a variation of the Iris convergent nozzle which yields a supersonic nozzle at the maximum jet area setting. This concept was conceived and tested by Grumman in a previous program; 3) C-D—a simulated convergent-divergent ejector with a schedule of exit to throat area, at each throat area, resulting in a maximum boat tail angle of 14°; 4) PLUG—a variable area plug nozzle[6] with a 10° half angle plug and cowl flaps scheduled to increase the exit area with increasing throat area; 5) BIDE—a Blow-In-Door Ejector[5] with an Iris primary nozzle and free floating doors and trailing edge flaps; 6) REF BIDE—a reference Blow-In-Door Ejector with doors fixed open, with a fixed ejector shroud and with a flap type convergent nozzle; and 7) END CAPS—circular arc, zero flow nozzle simulators instrumented with 40 area-weighted pressure taps. Secondary flow was not used in any of the nozzles. The four basic nozzles (IRIS, C-D, PLUG, BIDE) were tested at three jet area settings to simulate the effects of afterburning operation.

Results and Discussion

A complete tabulation of the basic measured data obtained at NASA—Langley is available.[13] The intent here is to complement these results using the newly defined interference parameters [Eqs. (1 and 2)].

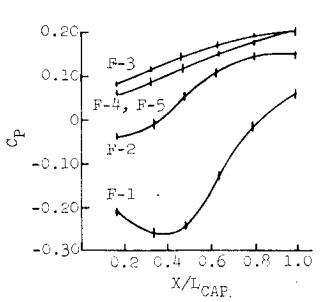

Fig. 7 Inboard pressure distribution.

Nozzle Simulator Tests

As indicated in Fig. 1a, a jet-off type simulation was used to obtain a reference drag D_{RF}. The end-cap (Figs. 1 and 5) connected to the internal supply pipe provided this effect. In addition, the pressure taps on the cap were used to obtain a nozzle simulator drag D_{CAP}. The end-cap geometry consisted of the same circular arc (radius equal to 4.2 engine diameters) as the IRS convergent nozzle, and the premise behind such a test was to obtain a qualitative assessment of the effect of placing nozzle surfaces in various aircraft flowfields. Results of these tests provided trends remarkably similar to most of the jet-on nozzle tests.

The reference fuselage drag (drag of metric empennage only) and end-cap drag shown in Fig. 6 illustrate two extremes in back-end performance. The F-1 fuselage drag is lower throughout the Mach number spectrum. Removing peripheral blockage, in the F-3 design, introduces slightly larger boattail angles on the rear fuselage with attendant increases in reference drag. However, the pressure integrated end-cap drag shows the reverse trend and large subsonic differences can be noted (Fig. 6) as well as negative end-cap drag values for the F-3 design. The net effect of these opposing drag trends is that the lower nozzle simulator drag more than compensates for the higher F-3 fuselage drag. As noted below, all nozzles placed in an F-1 type flowfield yielded large drag values at subsonic speeds. The inboard pressure distribution shown in Fig. 7 helps to explain this phenomenon and also indicates the recompression (positive C_P) on F-3 responsible for the negative drag values in Fig. 6. On Fig. 7, C_P is the standard pressure coefficient defined as (local pressure minus ambient pressure)/(freestream dynamic pressure).

Interference Drag at 0.8 Mach Number

Results for the five fuselages and six nozzle types at a high subsonic cruise Mach number (0.8) are displayed in Fig. 8. A carpet plot presentation is utilized to show the interference drag (normalized with respect to ideal nozzle thrust). These results indicate the following:

1) The performance of all nozzles becomes more favorable with decreasing peripheral blockage. This may be observed by following any line of constant nozzle type and noting the reductions in interference drag proceeding from the F-1 to F-3 fuselages.

2) All nozzles incur less drag as the spacing ratio increases. Note the lines of constant nozzle type proceeding from F-3 to F-5 installations

3) Favorable interference is possible in clean, widely spaced designs. Note the large negative values of D_{INT}.

4) Differences between nozzle type depend on the type of fuselage installation. Except for the F-1 design, the differences between nozzles become more noticeable in cleaner widely spaced configurations. This may be noted in Fig. 7 by following lines of constant fuselage and observing the steeper slopes proceeding from F-2 to F-5 fuselages.

5) The IRIS and C-D IRIS nozzles combined with a widely spaced design yields the lowest interference drag.

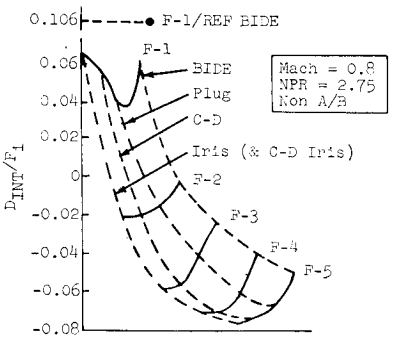

Fig. 8 Subsonic interference drag.

6) The F-1 type fuselage and REF Blow-In-Door Ejector (Fig. 4) was significantly poorer than all other cruise configurations.

7) The PLUG nozzle has the lowest interference drag in an F-1 type of installation.

Drag Components at 0.8 Mach Number

The results shown in Fig. 9 can be used to obtain all of the incremental drag items in Eqs. (2–4), at a high subsonic cruise Mach number (0.8). Shown in this graph are the nozzle drags ($\Delta F_{\diamond} + D_N$) for each of four basic nozzles in the five fuselage designs plotted as a function of the measured fuselage drag with the smallest (nonafterburning) nozzle area at a nozzle pressure ratio (NPR) of 2.75. The reference drag values are also shown for the five fuselages. All of the drag values are normalized with respect to freestream dynamic pressure times maximum cross-sectional area (A_{MAX}). From the data shown in Fig. 9, the following conclusions are obtained:

1) The nozzle type has a negligible effect on F-1 fuselage drag. Note that while each of the nozzles yield different values of ($\Delta F + D_N$), there is little effect on D_{BE}.

2) For fuselages other than the F-1, the nozzle type has a measurable effect on fuselage drag.

3) For all of the nozzles shown, the effect of the nozzle is to reduce fuselage drag relative to the reference configuration. Note that for all cases D_{BE} is less than or equal to D_{RF}. Thus, for this test series, ΔD was favorable.

4) The general trend for all fuselage/nozzle combinations was that the Blow-In-Door Ejector yields the lowest fuselage drag, but has the highest nozzle drag. The net effect is that the Blow-In-Door Ejector nozzle tested yielded the highest over-all drag ($\Delta F + D_N + D_{BE}$).

5) The nozzle effect on fuselage drag is most evident in clean widely spaced designs. Note that the total spread in D_{BE}, between highest and lowest drag, increases from F-1–F-4. This result indicates that with peripheral blockage and close spacing (F-1), the nozzle type can not as easily affect upstream fuselage pressures, whereas spreading the nozzles apart and eliminating peripheral blockage yields more fuselage area that can be affected by the nozzle type.

6) For most of the nozzle/fuselage combinations, the effect of fuselage flow on nozzle drag was favorable. For example, note that ($\Delta F + D_N$) is negative in the F-3–F-5 fuselages.

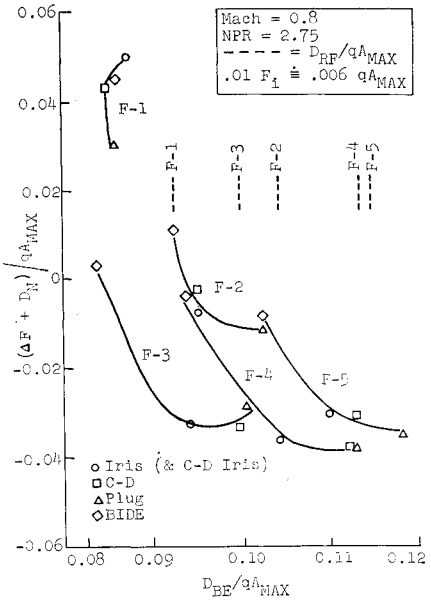

Fig. 9 Drag components.

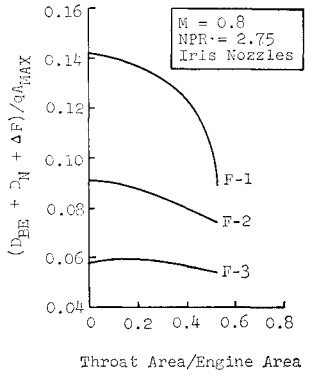

Fig. 10 Effect of jet area.

Effects of Jet Area

Figure 10 contains the effect of jet area on total drag ($D_{BE} + D_N + \Delta F$) for some of the fuselages, with an IRIS convergent nozzle at 0.8 Mach number. As noted previously, the end-cap can be considered as part of the IRIS design in the limit of zero jet area. Noteworthy in Fig. 10 is that while the fuselage/nozzle drag decreases with increasing jet area, nowhere is the effect as large as with the F-1 design. This trend is due to the nozzle shape and its environment. In fuselage F-1, the nozzle is in a low-pressure field (see Fig. 7) and decreasing the nozzle boat tail area (larger throat/engine area in Fig. 10) eliminates a large amount of drag. For fuselage F-3, the nozzle is in a positive pressure field and the effect is small in comparison to F-1.

Effect of Nozzle Pressure Ratio

Figure 11 contains results, typical of those obtained throughout the test program, on the effects of nozzle type and pressure ratio on fuselage drag. As noted in Fig. 11, these effects are measurable.

Increasing pressure ratio from jet-off conditions (NPR = 1) to a typical sonic pressure ratio (NPR = 1.9) decreases fuselage drag due to the jet filling the nozzle cavity (similar to base bleed). As the pressure ratio is increased (from 2 to 3) the jet velocity increases (without a substantial increase in plume size) and the drag increases due to entrainment of external flow by the jet. At higher pressure ratios (3 and above) the jet size increases substantially causing external flow blockage which feeds pressure upstream and decreases the drag. In general, fuselage drag did not vary much from the reference level (dashed line), except for the BIDE. This nozzle inhibits flow expansion in the vicinity of the customer connect (where nozzle meets fuselage) and thereby decreases the metric fuselage drag relative to other nozzles.

However it should be noted that Fig. 11 applies to fuselage forces only, and effects on nozzle drag are more pronounced. As previously discussed in Fig. 9, the BIDE drag more than offsets the low fuselage drag in Fig. 11.

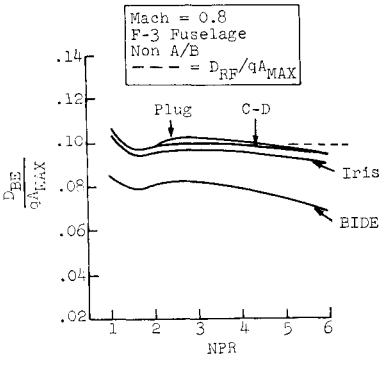

Fig. 11 Effect of nozzle pressure ratio.

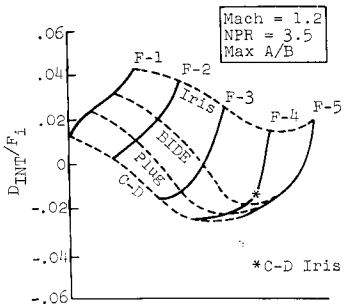

Fig. 12 Mach 1.2 interference drag.

Interference Drag at Supersonic Speeds

The matrix of interference data obtained at 1.2 Mach number and maximum jet area shown in Fig. 12 is typical of the trends obtained at low supersonic speeds. It can be noted that at these conditions; 1) the effect of nozzle type is much more pronounced than the fuselage installation effects, 2) nozzle performance continues to improve with reductions in peripheral blockage (F-1, F-2, F-3) whereas spacing appears to have less of an effect (F-3, F-4, F-5), and 3) the simple convergent IRIS has the highest drag, whereas nozzles better suited for supersonic operation result in decreased drag (less boat tail area and increased exit area).

Similar effects of fuselage design on nozzle performance were also obtained at 2.2 Mach number. It is interesting to note that even at 2.2 Mach number, the effect of nozzle type on fuselage drag was still measurable.

The sum of internal nozzle efficiency (C_V) and interference drag is denoted as equivalent thrust[10] which is shown in Fig. 13 for a range of nozzles and fuselages at 2.2 Mach number. At these conditions, the nozzle area ratios (exit/throat) were 1.0, 1.35, 1.73, 2.29 (doors closed), and 1.25 for the IRIS, C-D, PLUG, BIDE, and C-D IRIS, respectively. From Fig. 13, the following is noted:

1) The IRIS convergent nozzle induces a substantial favorable interference, presumably due to the large plume. Note that C_{TEQ} is greater than C_V in all installations.

2) On an installed basis, the favorable interference for a convergent nozzle is more than offset by the higher internal performance of the other type nozzles.

3) A small area ratio C-D Iris nozzle performs as well as the larger area ratio supersonic nozzles (C-D, PLUG, BIDE).

4) The interference drag is not greatly affected by fuselage design so that the relative merits among nozzles remains substantially the same in each fuselage.

Conclusions

1) For all nozzle types investigated, large performance differences were obtained at subsonic conditions due to twin-jet fuselage design and upstream maximum body area. These differences in nozzle performance render nozzle studies useless without detailed knowledge of the aircraft flowfield.

2) The nozzle type has a measurable effect on fuselage forces at subsonic and supersonic flight conditions.

3) At subsonic cruise conditions: a) a clean fuselage installation is the key factor in reducing interference drag and wide spacing is beneficial; b) clean widely spaced designs yield minimum interference drag with all nozzle types and the differences between nozzle designs are more pronounced; and c) closely spaced designs with large amounts of peripheral blockage are most sensitive to changes in nozzle throat and exit area.

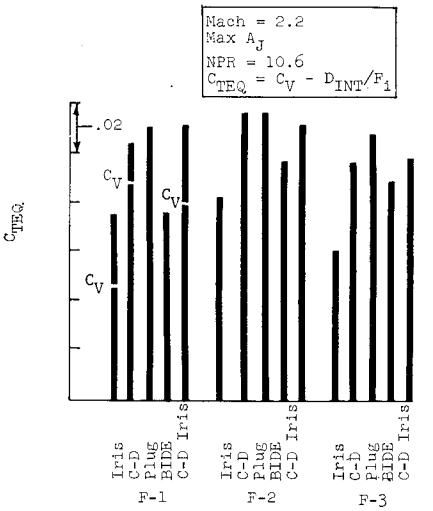

Fig. 13 Equivalent thrust at 2.2 Mach number.

4) At supersonic maximum jet area conditions, the internal nozzle geometry is the most important factor for increasing performance. A small area ratio convergent–divergent nozzle yields excellent installed performance.

References

[1] Nichols, M. R., "Aerodynamics of Airframe-Engine Integration of Supersonic Aircraft," TN D-3390, 1966, NASA.

[2] Armstrong, R. S. and Miller, S. R., "Subsonic Aerodynamic Performance of Nozzle Installations in Supersonic Airplanes," AIAA Paper No. 67-452, Washington, D. C., 1967.

[3] Motycka, D. and Skowronek, P. J., Jr., "Use of Statistically Designed Experiments in Wind-Tunnel Test Program," *Journal of Aircraft*, Vol. 4, No. 4, July–Aug. 1967.

[4] Greathouse, W. K., "Blending Propulsion with Airframe," *Space/Aeronautics*, Nov. 1968.

[5] Migdal, D. and Horgan, J. J., "Thrust Nozzles for Supersonic Transport Aircraft," *Transactions of the ASME, Series A*, Vol. 86, No. 2, April 1964.

[6] Rabone, G. R. and Harshman, D. L., "Low Angle Plug Nozzle Performance Characteristics," AIAA Paper 66-664, Colorado Springs, Colo., 1966.

[7] Corson, B. W., Jr., and Schmeer, J. W., "Summary of Research on Jet-Exit Installation," TM X-1273, 1966, NASA.

[8] Runckel, J. F. and Swihart, J. M., "A Hydrogen Peroxide Simulator for Wind Tunnel Tests of Turbojet Exit Models," MEMO 1-10-59L, Feb. 1959, NASA.

[9] Shrewsbury, G. D., "Effect of Boattail Juncture Shape on Pressure Drag Coefficients of Isolated Afterbodies," TMX-1517, March 1968, NASA.

[10] Migdal, D. and Greathouse, W. K., "Optimizing Exhaust-Nozzle/Airframe Thrust Minus Drag," 680294, April 1968, Society of Automative Engineers.

[11] Schaeffer, W. T., Jr., "Characteristic of Major Active Wind Tunnels at the NASA Langley Research Center," TMX-1130, July 1965, NASA.

[12] Capone, F. J. and Putnam, L. E., "Pressure Distributions, Boundary Layer Profiles and Drag Characteristics for a Cylindrical Afterbody Tested on the Strut-mounted Air-Powered Nacelle at Mach Numbers from 1.16 to 2.60," LWP-569, Feb. 1968.

[13] Mercer, C. E. and Berrier, R. L., "Effect of Afterbody Shape, Nozzle Type, and Engine Lateral Spacing on the Installed Performance of a Twin Jet Afterbody Model." TMX-1855, Sept. 1969, NASA.

[14] Grumman Aircraft Pretest Report, "1/12 Scale Models for NASA LRC 16 Foot and 4 Foot Wind Tunnels," AER/TPT-24, March 1968.

SYNOPTIC: A Simplified Method of Estimating the Response of Light Aircraft to Continuous Atmospheric Turbulence, E. L. Peele and R. Steiner, NASA Langley Research Center, Hampton, Va.; *Journal of Aircraft*, Vol. 7, No. 5, pp. 402–407.

Aircraft Gust Response: Random Atmosphere Turbulence

Nomenclature

$C_{L\alpha}$ = wing lift-curve slope
$\bar{c}$ = reference wing chord, ft
$k_{0\alpha}$ = reduced frequency
S = wing area, ft^2
s = $2L/\bar{c}$
L = internal gust scale, ft
g = acceleration due to gravity
U = airspeed, fps
U_{de} = derived gust velocity, fps
ρ_0 = air density at sea level
w = airplane weight, lb
$\sigma_{\Delta n}$ = rms load factor, g's
σ_w = rms gust velocity, fps
V_e = equivalent airspeed

Theme

Formulas are presented for mixing estimates of the response of light general aviation aircraft to random atmospheric turbulence. The numerical calculations involved are facilitated through the use of parametric charts of certain key integrals. These integrals are functions of the basic aircraft stability characteristics and the gust scale.

Content

Random gust response calculations are based on two quantities, $\bar{A}_y$ and N_0, which express, respectively, the ratio of some rms response σ_y to the rms gust velocity σ_y and the number of times per unit time that y crosses the value of zero with positive slope. Equations for the quantities are

$$\bar{A}_y = \frac{\sigma_y}{\sigma_g} = \left\{\left[\int_0^\infty \Phi_y(\omega)d\omega\right]\Big/\left[\int_0^\infty \Phi_g(\omega)d\omega\right]\right\}^{1/2} \quad (1)$$

$$N_0 = \frac{1}{2\pi}\left\{\left[\int_0^\infty \Phi_y(\omega)\omega^2 d\omega\Big/\int_0^\infty \Phi_y(\omega)d\omega\right]\right\}^{1/2} \quad (2)$$

where $\Phi_y = |H(\omega)|^2\Phi_g(\omega)$.

After imposing a number of simplifying assumptions regarding aircraft size, flexibility and rigid body response characteristics, formulas applicable to light aircraft are derived. As an example, consider the normal load factor resulting from a vertical gust input. The formulas are

$$\bar{A}_n = \zeta_\alpha\omega/g\gamma_\alpha\{R_\beta{}^4 + 4\zeta_\alpha{}^2[1 - (1/\gamma_\alpha)]^2R_\beta{}^2\}^{1/2} \quad (3)$$

$$N_0 = \frac{\omega_{0\alpha}}{2\pi}\left[\frac{R_\beta{}^6 + 4\zeta_\alpha{}^2[1 - (1/\gamma_\alpha)]^2R_\beta{}^4}{R_\beta{}^4 + 4\zeta_\alpha[1 - (1/\gamma_\alpha)]^2 R_\beta{}^2}\right] \quad (4)$$

γ_α = dimensionless damping force parameter, ζ_α = damping ratio, $\omega_{0\alpha}$ = short-period undamped frequency, and $R_{\beta^{(j)}}$ = response integrals.

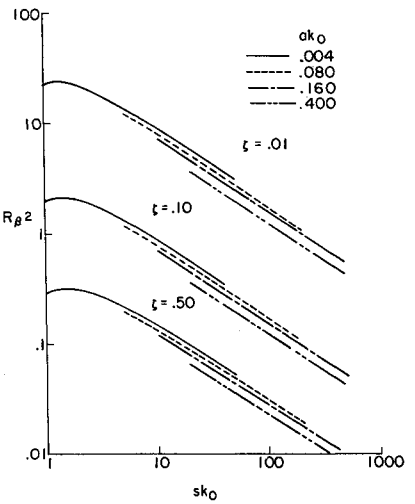

Fig. 1 Response integral, $R_B{}^2$.

The response integrals $R_{\beta^{(j)}}$ are of the form

$$R_{\beta^{(j)}} = \frac{sk_0}{\pi}\int_0^\infty \frac{\beta^j e^{-ak_0\beta}[1 + \frac{8}{3}(1.339sk_0\beta)^2]d\beta}{[(1 - \beta^2)^2 + 4\zeta^2\beta^2][1 + \frac{8}{3}(1.339sk_0\beta)^2]^{\frac{11}{6}}}$$

and have been evaluated over a suitable range of the arguments: damping ratio ζ, gust relative scale parameters sk_0 and ak_0, a parameter representing the unsteady lift function due to gust impingement. The numerical evaluations of the response integrals are presented as parametric charts (Fig. 1).

Estimates of both longitudinal and lateral load and motion responses to independently applied vertical and lateral gusts can be made by use of the formulas and charts.

The formulas are shown to be analogous to the discrete gust formulas where the factor K_Φ is of a similar nature as K_g.

Sample calculations are included to illustrate the application of the formulas:

discrete gusts:

$$\Delta n_{\max}/U_{de} = (\rho_0 SV_eC_{L\alpha}/2w)\,K_g,$$
$$Kg = 0.88\,\mu g/(5.3 + \mu g), \quad \mu g = 2w/g/\rho S\bar{c}C_{L\alpha}$$

spectral:

$$\sigma_{\Delta n}/\sigma_w = (\rho SUC_{L\alpha}/2w)\,K_\Phi,$$
$$K_\Phi = \{R_\beta{}^{4^2} + 4\zeta_\alpha{}^2[1 - (1/\gamma)]^2R_\beta{}^{2^2}\}^{1/2}$$